



CHORUS

This is the accepted manuscript made available via CHORUS. The article has been published as:

Anharmonic phonon renormalization and thermal transport
in the type-I $\text{Ba}_8\text{Ga}_{16}\text{Sn}_{30}$ clathrate from first principles

$\text{Ba}_8\text{Ga}_{16}\text{Sn}_{30}$ clathrate from first principles

Masato Ohnishi, Terumasa Tadano, Shinji Tsuneyuki, and Junichiro Shiomi

Phys. Rev. B **106**, 024303 — Published 8 July 2022

DOI: [10.1103/PhysRevB.106.024303](https://doi.org/10.1103/PhysRevB.106.024303)

Anharmonic Phonon Renormalization and Thermal Transport in Type-I $\text{Ba}_8\text{Ga}_{16}\text{Sn}_{30}$ Clathrate from First Principles

Masato Ohnishi^{1,*}, Terumasa Tadano^{2,3}, Shinji Tsuneyuki^{4,5}, and Junichiro Shiomi^{1,*}

¹*Department of Mechanical Engineering, The University of Tokyo, 7-3-1, Hongo, Bunkyo-ku, Tokyo 113-8656, Japan*

²*Research Center for Magnetic and Spintronic Materials, National Institute for Materials Science (NIMS), 1-2-1 Sengen, Tsukuba, Ibaraki 305-0047, Japan*

³*Elements Strategy Initiative Center for Magnetic Materials, National Institute for Materials Science (NIMS), 1-2-1 Sengen, Tsukuba, Ibaraki 305-0047, Japan*

⁴*Department of Physics, The University of Tokyo, 7-3-1, Hongo, Bunkyo-ku, Tokyo 113-0033, Japan*

⁵*Institute for Solid State Physics, The University of Tokyo, 5-1-5, Kashiwanoha, Kashiwa, Chiba 277-8581, Japan*

Effects of strong phonon anharmonicity of a type-I clathrate $\text{Ba}_8\text{Ga}_{16}\text{Sn}_{30}$ induced by quadruple-well potential of guest atoms were investigated. Phonon transport including coherent interbranch component was analyzed using a first-principles-based self-consistent phonon (SCP) theory that gives temperature-dependent harmonic interatomic force constants and by solving off-diagonal components of group velocity operator. Experimentally observed thermal conductivities have been reasonably reproduced by considering both lattice and electron contributions. Through the analysis with the SCP theory, we found that hardening of guest modes leads to an increase in lattice thermal conductivity at frequencies below those of framework-dominant flat modes ($< 40 \text{ cm}^{-1}$), which finally results in the slow decay of the total lattice thermal conductivity with increasing temperature. Detailed analyses revealed that the increase in lattice thermal conductivity at low frequency is attributed to (a) the increase in both of group velocities and lifetimes of phonon modes located at frequencies below that of the flat guest modes and (b) abnormal increase in lifetimes of phonon modes located between frequencies of the flat guest and framework modes with increasing temperature.

I. INTRODUCTION

Phonon-glass electron-crystal [1] is a concept of ideal thermoelectric properties of crystal materials. Materials such as skutterudite [2], perovskite [3,4], and clathrate compounds [5,6] composed of cages and guest atoms are expected to realize this concept. In these materials, it is expected that phonons are significantly scattered by guest atoms while electrons can transport in the framework without significant scattering. Because a large free space of guest atoms is preferred to enhance phonon scattering by guest atoms [7,8], type-I clathrates [9] composed of Weaire-Phelan structure [10], which divides space into cage structures with a large volume, may be the most promising material. Indeed, they exhibit various intriguing phonon properties such as a glass-like plateau of temperature-dependent thermal conductivity, $\kappa(T)$, at low temperatures [7,11,12], significant hardening of guest modes with temperature [13–15], and weak temperature dependence of $\kappa(T)$ at high temperatures [7,12,16].

* ohnishi@photon.t.u-tokyo.ac.jp, shiomi@photon.t.u-tokyo.ac.jp

Recent theoretical works on clathrates have revealed the basic effects of the guest atoms on phonon properties. The weak interaction between guest atoms and the framework results in flat bands, and the flat guest bands affect phonon properties in different manners. The main impact of the flat guest bands on phonon properties is to suppress phonon relaxation times in a wide range of frequencies [17–19]. It may be straightforward to understand that the flattening of bands increases scattering phase space (SPS) of phonons and decreases their relaxation time. In addition to SPS, the three-phonon coupling matrix represented by eigenvalues, polarization vectors, and atomic masses (described in Methodology in detail) among scattered phonons also has a vital role in decreasing the relaxation time according to detailed analyses on type-I $\text{Ba}_8\text{Ga}_{16}\text{Ge}_{30}$ (BGGe) [19]. As for phonon group velocity, while hybridization of the guest modes and framework modes decreases group velocities, theoretical works [18,19] have shown that the effect on group velocities is secondary. It has also been found that the glass-like plateau of temperature-dependent thermal conductivity at low temperature can be attributed to thermal excitation of phonons with higher frequencies than those of flat bands [20]. It may be interesting to note that the glass-like plateau is not a direct consequence of phonon anharmonicity because the effect of thermal excitation is relatively enhanced by the flat guest bands that suppress the contribution of low-frequency phonons to heat transport. Therefore, an in-depth understanding of the phenomena observed at high temperatures, e.g., the weak temperature dependence of thermal conductivity, should give us more knowledge on phonon anharmonicity.

In this study, we investigate the effects of strong phonon anharmonicity at high temperatures from first-principles calculations. Type-I clathrate $\text{Ba}_8\text{Ga}_{16}\text{Sn}_{30}$ (BGSn), which has a remarkably strong anharmonicity [21] compared with other off-center clathrates such as Sr- and Eu-filled Ge clathrates ($\{\text{Sr}/\text{Eu}\}_8\text{Ga}_{16}\text{Ge}_{30}$) [22], is mainly analyzed. Furthermore, type-I $\text{Ba}_8\text{Ga}_{16}\text{Si}_{30}$ (BGSi), which has much weaker anharmonicity than BGSn, is analyzed to highlight the effect of strong anharmonicity in BGSn. Quartic phonon anharmonicity is incorporated to obtain temperature-dependent *effective* second-order interatomic force constants (IFCs) using a self-consistent phonon (SCP) theory [23,24]. In addition to the phonon transport considered by the Peierls-Boltzmann transport equation (BTE), the coherent interbranch component is also considered by employing the so-called unified theory formulated by Simoncelli *et al.* [25]. These analyses reveal that lattice thermal conductivity can be increased by hardening of flat-band guest modes and the coherent thermal transport is not negligible above a few hundred degrees Kelvin. Because the hardening of guest modes significantly increases thermal conductivity at low frequencies, it leads to intriguing phenomena such as stronger suppression of thermal conductivity due to nanostructuring at higher temperatures.

II. METHODOLOGY

A. Interatomic Force Constants

Type-I clathrate BGSn with a highly symmetric structure ($Pm\bar{3}n$ space group) was analyzed in this study. For the sake of comparison, type-I BGSi, which has much weaker anharmonicity than type-I BGSn, was also analyzed. In the both structures, all the $16i$ sites are occupied by gallium atoms and the $6c$ and $24k$ sites are occupied by tin atoms. IFCs were obtained with first-principles calculations using the *Vienna ab initio simulation package* (VASP) [26]. Perdew-Burke-Ernzerhof exchange-correlation functional [27] with the projector augmented wave potential [28,29] was employed in all the calculations. The cutoff energies were set at 330 and 340 eV for BGSi and BGSn, respectively. The lattice constants

1 of the clathrates were optimized using a $4 \times 4 \times 4$ Monkhorst–Pack k -mesh, where k is the wavevector. The optimized
 2 lattice constants were 10.60 Å for BGSi and 11.90 Å for BGSn. While the former value is in excellent agreement with an
 3 experimental value (10.59 Å [30]), the latter is slightly larger than an experimental value (11.69 Å [31]). While the lattice
 4 thermal conductivity may depend on the value of the lattice constant[20], the values obtained through calculations of this
 5 study are used herein.

6 To obtain anharmonic IFCs of BGSn, many structures in which atoms were randomly displaced, were prepared,
 7 while harmonic IFCs were obtained through a finite displacement approach [32] with a displacement of 0.01 Å. $2 \times 2 \times$
 8 2 supercells, containing 432 atoms, were used for BGSn to calculate IFCs while primitive cells were used for BGSi to
 9 reduce the computational cost. First, first-principles molecular dynamics (MD) simulations with a primitive cell were
 10 performed at a temperature of 500 K with a time step of 1.0 fs and a $2 \times 2 \times 2$ Monkhorst–Pack k -mesh. The temperature
 11 was controlled using a velocity-scaling algorithm during the first few hundred femtoseconds of the simulation and then
 12 via the Nosé–Hoover algorithm [33]. After confirming that atomic vibrations had stabilized, the structures were extracted
 13 every 50 fs, and every atom was displaced along a random direction with a maximum magnitude of 0.1 Å to ensure that
 14 no two structures were correlated. More than 120 structures were prepared from the trajectory of the MD simulation.
 15 Using the set of atomic displacements and forces, anharmonic IFCs were calculated up to the sixth order using the least
 16 absolute shrinkage and selection operator solved using the coordinate descent method [34], while the harmonic IFCs were
 17 fixed with those obtained by the finite displacement method. The cutoffs of IFCs were set to be 20.6 and 5.29 Å for
 18 harmonic and other orders, respectively, and interactions of atoms were considered up to three, two, and two body for
 19 fourth-, fifth-, and sixth-order IFCs, respectively. In the case of BGSn, after the calculation of IFCs with the primitive
 20 cell, IFCs were calculated with a $2 \times 2 \times 2$ supercell with a similar manner while IFCs obtained with the primitive cell
 21 were used to perform a MD simulation for the supercell, more than 180 randomly displaced structures were prepared to
 22 calculate forces on atoms, and $2 \times 2 \times 2$ Monkhorst-Pack k -mesh was employed for first-principles calculations.
 23 Temperature-dependent harmonic IFCs were obtained by using the self-consistent phonon (SCP) theory [20,23] that
 24 modifies harmonic IFCs with the effect of quartic anharmonicity. The SCP calculations were performed at the Γ point (q
 25 $= 0$), and eigenvectors at arbitrary q points were obtained via Fourier interpolation. Because only short-range interactions
 26 contribute to anharmonic terms, the Γ point calculation should be sufficient for this study. For all the simulations based
 27 on the SCP theory, off-diagonal components of self-energy and, thus, polarization mixing were considered in this study.
 28 Also, while it is, in principle, possible to update the atomic positions at each temperature within a self-consistent phonon
 29 formulation [35], we do not consider this effect in this study due to computational limitations and assume that the atomic
 30 positions do not change from their equilibrium positions at 0 K. Notwithstanding, the present SCP method should be
 31 useful for understanding anharmonic lattice dynamics and thermal transport of BGSn at relatively high temperatures
 32 above ~ 100 K, where the kinetic energy surpasses the depth of the multiple-well potential inside the host cage and thereby
 33 makes the effect of off-centering motion becomes less significant.

34 B. Lattice Thermal Conductivity

35 Using the obtained harmonic and cubic IFCs, lattice thermal conductivity, κ_L , without including the coherent part, κ_p ,

1 was calculated by solving Peierls-BTE, which is associated with diagonal terms of group velocity operator [36].
 2 Considering the second-order perturbation within the single-mode relaxation approximation, the linewidth due to the
 3 three-phonon scattering for phonon mode q is derived as

$$4 \quad \Gamma_q = \frac{\pi}{16N} \sum_{q_1, q_2} |V_3(-q, q_1, q_2)|^2 [(n_1 + n_2 + 1)\delta(\omega_q - \omega_1 - \omega_2) - 2(n_1 - n_2)\delta(\omega_q - \omega_1 + \omega_2)], \quad (1)$$

5 where the subscripts ($i = 1, 2$) denote phonon modes contributing to the scattering of the target mode q , n_i is the Bose-
 6 Einstein distribution function, ω_i is the phonon frequency, N is the number of \mathbf{q} points, and $\pm q = (\pm \mathbf{q}, s)$ with \mathbf{q} and s
 7 being the wavevector and branch index, respectively. The three-phonon coupling matrix element V_3 is given by

$$8 \quad V_3(q, q_1, q_2) = \left(\frac{\hbar}{\omega \omega_1 \omega_2} \right)^{\frac{1}{2}} \times \sum_{\mathbf{R}_i l_i p_i} \Psi_{0l_0, \mathbf{R}_1 l_1, \mathbf{R}_2 l_2}^{p_0 p_1 p_2} \times \frac{\mathbf{e}_{l_0}^{p_0}(q) \mathbf{e}_{l_1}^{p_1}(q_1) \mathbf{e}_{l_2}^{p_2}(q_2)}{\sqrt{M_{l_0} M_{l_1} M_{l_2}}} \times \exp[i(\mathbf{q} \cdot \mathbf{R}_0 + \mathbf{q}_1 \cdot \mathbf{R}_1 + \mathbf{q}_2 \cdot \mathbf{R}_2)], \quad (2)$$

9 where \hbar is the reduced Planck constant, \mathbf{R}_i is the position of the primitive cell, l_i is the atom index, p_i is the direction of
 10 the displacement of atom l_i , M is the atomic mass, Ψ is the cubic IFCs, and $\mathbf{e}(q)$ is the eigenvector of the mode q . The
 11 phonon lifetime due to three phonon scattering τ_{pp} is given by $\tau_{pp}(q) = 1/(2\Gamma_q)$. The total phonon lifetime of mode q
 12 is obtained with Matthiessen's rule: $\tau_q^{-1} = \tau_{q,pp}^{-1} + \tau_{q,iso}^{-1} + \tau_{q,b}^{-1}$, where $\tau_{q,iso}^{-1}$ is the scattering rate due to isotopes [37],
 13 and $\tau_{q,b}^{-1} = 2|\mathbf{v}_q|/L_g$ due to boundary of grains with an effective diameter L_g , respectively. Finally, the Peierls term is
 14 calculated as $\kappa_p^{\alpha\beta, scp}(T) = (NV)^{-1} \sum_q c_q(T) v_q^\alpha(T) v_q^\beta(T) \tau_q(T)$ using IFCs modified with SCP theory. Here, V is the
 15 volume of the primitive unit cell, c is the mode specific heat, v is the group velocity, and α and β are the Cartesian
 16 directions. In this analysis, the result for $\alpha = \beta$ was taken because the type-I clathrates used were isotropic.

17 Because linewidths of phonons may be larger than interbranch spacings in some branches of BGSn, the contribution
 18 of interbranch coherent tunneling to heat transport may not be negligible. Therefore, the coherent component,
 19 corresponding to the nondiagonal terms of the heat flux operator, was calculated by the unified theory [25,36]. Its
 20 contribution can be obtained as

$$21 \quad \kappa_c^{\alpha\beta} = \frac{\hbar^2}{k_B T^2 V N} \sum_q \sum_{s_1 \neq s_2} \frac{\omega_1 + \omega_2}{4} V_{12}^\alpha(\mathbf{q}) V_{21}^\beta(\mathbf{q}) \frac{\omega_1 n_1 (n_1 + 1) + \omega_2 n_2 (n_2 + 1)}{(\omega_1 - \omega_2)^2 + (\Gamma_1 + \Gamma_2)^2} (\Gamma_1 + \Gamma_2), \quad (3)$$

22 where k_B is the Boltzmann constant. The subscripts (1 and 2) denote the phonon modes (\mathbf{q}, s_1) and (\mathbf{q}, s_2) , respectively.
 23 The generalized group velocity operator $V(q)$ is given as

$$24 \quad V_{12}(\mathbf{q}) = \frac{1}{\omega_1 + \omega_2} \left\langle \mathbf{e}(q_1) \left| \frac{\partial D(\mathbf{q})}{\partial \mathbf{q}} \right| \mathbf{e}(q_2) \right\rangle, \quad (4)$$

25 where $D(\mathbf{q})$ is the dynamical matrix, which includes the anharmonic renormalization from the SCP theory.

26 Both for the Peierls and coherent contribution, κ_L were calculated with $N_q \times N_q \times N_q$ \mathbf{q} -meshes, where N_q was
 27 varied from 11 to 19, and final values were obtained by a linear extrapolation with respect to N_q^{-1} . The tetrahedron method

[38] was used for the integration over the Brillouin zone. For the above simulations to obtain IFCs and $\kappa_L (= \kappa_p^{\text{SCP}} + \kappa_{\text{off}})$, ALAMODE package [3,39] was employed.

C. Electron Thermal Conductivity

Because electron contribution to thermal transport may not be negligible in BGSn above room temperature [40], electron thermal conductivity, κ_{el} , was also calculated within the constant relaxation time approximation employing BoltzTrap2 [41]. Details are also documented in Sec. I of Supplementary Materials (SM) [42]. Electron band structures were calculated using VASP in basically the same manner as that for the phonon analysis. The \mathbf{k} -mesh density was set to $20 \times 20 \times 20$ for electron analysis, with which the convergence of electron properties such as electrical conductivity was confirmed. The carrier concentration is set to be an experimentally observed value, $3.2 \times 10^{18} \text{ cm}^{-3}$ [31], and the electron relaxation time was determined as 1.26 fs to reproduce the electrical conductivity at room temperature [31].

The principal reason to consider electron contribution is to reproduce an increase in thermal conductivity above room temperature due to the bipolar effect [40]. Although the temperature at which the bipolar effect becomes distinct strongly depends on the magnitude of the band gap, the accurate investigation of the band gap of clathrates is challenging. This difficulty comes from a unique feature of clathrates as well as a general problem of semilocal density functionals for exchange and correlation [43]. In the framework of clathrate compounds, atoms can be placed with different combinations of sites and elements, namely site occupancy factors, even with the same composition of elements, and their electronic states depend on the placement of atoms [44,45]. While it may be possible to estimate a plausible band gap by considering the effect of temperature and taking an ensemble average for possible structures [46–48] and carefully selecting an exchange-correlation functional, we simply modified the magnitude of band gap by manually adjusting the energy of the conduction bands in this analysis. This adjustment of the band gap modifies only the threshold temperature of bipolar effect, but not the increasing rate of electron thermal conductivity with temperature, as shown in Fig. S1 in SM.

III. RESULTS AND DISCUSSIONS

A. Temperature-dependent Harmonic Properties

Because type-I BGSn has a quadruple-well potential on Ba guest atom at $6d$ site, the quartic lattice anharmonicity and the associated temperature renormalization of phonon frequency are significant. Figure 1(a) shows a potential energy surface (PES) of the lowest optical mode at the Γ point (T_{2g} mode), which is dominated by the guest atom. The deviation of the stable positions of the guest atom from the cage center was 0.84 \AA that exceeded an experimental value of 0.43 \AA [31]. This overestimation should be because of the larger lattice constant as mentioned in Sec. II A. The depth of the quadruple-well potential was 5.6 meV/atom (0.31 eV/unit), which corresponds to 66 K . Decomposed anharmonic contributions up to sixth-order show that even-order potentials dominate the potential on the guest atom at $6d$ site while the odd-order potentials become zero because of the symmetry. By employing the SCP theory, harmonic IFCs (blue dotted lines in Fig. 1(a)) were gradually renormalized by the quartic potential (red dash-dotted line) with increasing the temperature. Under the assumption used in this analysis assuming that guest atoms vibrate on the cage center in a positive harmonic potential, the SCP calculation is converged only above a certain temperature at which the effective harmonic

1 potential including the effect of quartic potential becomes positive. In this study, the SCP calculation is converged above
 2 100 K for the type-I BGSn. While eigenvalues have imaginary values without considering the effect of quartic
 3 anharmonicity, an inclusion of quartic anharmonicity lifts imaginary frequencies to positive values, as shown in Fig. 1(b).
 4 Following the hardening of phonon modes, the frequency of T_{2g} mode (the lowest optical mode) is varied from 6.2 cm^{-1}
 5 at 100 K to 13 cm^{-1} at 300 K, as shown in Fig. S2(a) in SM. The experimentally-measured frequencies of T_{2g} mode are
 6 16 cm^{-1} at 100 K and 19 cm^{-1} at 300 K [15,49]. This comparison shows that while the discrepancy between the
 7 experimental and theoretical values is distinct at low temperatures, it becomes smaller with increasing temperature. The
 8 underestimation of the frequencies of the rattling modes may be attributed to the overestimation of the lattice constant.
 9 Another possibility is that the instability of the highly symmetric structure used in this study [44] may soften some phonon
 10 modes including the guest modes. Indeed, our simulation with a lower symmetric, but more stable, structure shows higher
 11 frequencies of the guest modes and a larger split of their frequencies, which agree with the experimental data while we
 12 employed the symmetric structure for the simplicity in this study. Calculation of partial density of states (DOS) shows
 13 that flat modes lying at low frequency can be divided into two groups, as shown in Figs. S2(b) and S2(c) in SM, which
 14 show clearer phonon dispersion and DOS. The flat bands around 20 cm^{-1} are dominated by Ba guest atoms while flat
 15 bands around $40\text{-}60 \text{ cm}^{-1}$ are dominated by the framework. We will show that phonon modes located at a frequency below
 16 the flat guest bands and phonon modes located between the flat guest and framework modes play an important role in
 17 realizing intriguing phonon properties of type-I BGSn.

18 B. Temperature-dependent Thermal Conductivity

19 Using the temperature-dependent effective harmonic IFCs and (bare) cubic IFCs, thermal conductivities of type-I BGSn
 20 were calculated. Because κ_L linearly increased with decreasing N_q^{-1} both for Peierls and coherent contributions [50], as
 21 shown in Fig. S3, final values were obtained by a linear extrapolation with respect to N_q^{-1} . While SCP calculations were
 22 not converged below 100 K, available data are shown in Fig. 2. Data on solid lines were obtained by the extrapolation
 23 while those of a dotted line were for $N_q = 11$. To reproduce the increase of thermal conductivity above 300 K observed
 24 in the experiment [40], the electronic band gap was modified from 0.045 to 0.06 eV for the extrapolated data and to 0.15
 25 eV for data of $N_q = 11$. The result shows that total thermal conductivities including Peierls, coherent, and electron
 26 contributions (squares with solid line) overestimate experimental data in the overall temperature while data obtained with
 27 $N_q = 11$ can reproduce them. Possible missing factors in this analysis which reduce thermal conductivity may be
 28 dynamical disorder of guest atoms [16,51], four-phonon scattering [52,53], or thermal expansion [20,48]. While the
 29 dynamical disorder mainly affects thermal conductivity at low temperatures, other two factors should decrease thermal
 30 conductivities in the overall temperature. We would like to note that $N_q = 11$ is not a small size of q -mesh compared
 31 with previous calculations [20,48]. This indicates that it is still challenging to reveal all the physics behind the small
 32 thermal conductivity of clathrate compounds. As for the Coulomb interaction among guest ions, we did not consider the
 33 dipole-dipole interaction beyond the $2 \times 2 \times 2$ supercell in this study while it may affect thermal conductivity at low
 34 temperatures [54,55].

35 We would like to also comment on the difference between the temperature dependences of thermal conductivity of

1 amorphous structures and off-center type-I clathrates, that is, that of glasses and the glass-like dependence. κ_L of glasses
2 keeps increasing in all the temperature region except for at low temperatures (typically around 10 K), at which its
3 temperature dependence is absent, and at temperatures above the high temperature limit (typically around 100 K), at
4 which it saturates a certain value [56]. The same temperature dependence has been observed in type-I clathrate compounds
5 with large off-center distances such as $\text{Sr}_8\text{Ga}_{16}\text{Ge}_{30}$ [16] and $\text{Eu}_8\text{Ga}_{16}\text{Ge}_{30}$ [57] as well as BGSn [31]. While we targeted
6 temperatures above 100 K, at which equilibrium positions of guest atoms should be considered as the center of cage
7 structure, our results in Fig. 2 and experimental data of type-I BGSn [31,40] show that κ_L of off-center type-I clathrate
8 can decrease after taking the maximum value at around 100 K. Our simulations reveals the difference of physics on heat
9 transport at high temperatures between amorphous and off-center type-I clathrate. While heat transport is dominated by
10 diffusons and locons in amorphous systems, it is still dominated by propagons (κ_p^{SCP} in this study) at high temperatures
11 (> 100 K) in off-center type-I clathrate. Because the temperature dependence of the total κ_L is **dominated** by competing
12 temperature dependences of propagons and other contributions, diffusons and locons (**dominant factors of κ_{off}** in this
13 study), when propagons mainly contribute to κ_L , the total κ_L decrease due to increase in phonon-phonon scattering with
14 increasing temperature. It may be interesting to think that, while thermal properties of off-center clathrate is glass-like at
15 low temperatures, it turns back to crystal at high temperatures because of its high order anaharmonicicity.

16 While a few physics may still be unveiled, our calculations show intriguing thermal properties of clathrate
17 compounds: (a) slow reduction of lattice thermal conductivity with temperature ($\propto T^{-0.36}$), (b) significant contribution
18 of coherent component, and (c) sharp increase in thermal conductivity because of electronic contribution. While the
19 increase of κ_{el} might be noticeable, its effect simply can be attributed to the bipolar effect (see Fig. S1 in SM). We will,
20 therefore, focus on more intriguing phenomena of phonon transport below.

21 C. Modal Thermal Conductivity

22 To gain insight into the slow decay of $\kappa(T)$ with temperature, spectral and cumulative $\kappa_p^{\text{SCP}}(T)$ of type-I BGSi and BGSn
23 are compared in Fig. 3. In usual single-crystal materials, including type-I BGSi, that do not have strong phonon
24 anharmonicity, modal thermal conductivity decreases with increasing temperature at most frequencies because of the
25 enhancement of phonon-phonon scattering, as shown in Fig. 3(a). In type-I BGSn, interestingly, thermal conductivities
26 at low frequency (below 50 cm^{-1}) increases with the temperature, as shown in Fig. 3(b). This increase of thermal
27 conductivity of low-frequency phonons partially compensates the decrease of heat transport of higher-frequency phonons
28 ($> 50 \text{ cm}^{-1}$), leading to the weak temperature dependence. Thermal conductivity divided into different frequency ranges
29 show distinctly different features in BGSi and BGSn, as shown in Fig. S4. In BGSi, lower-frequency phonons ($< 50 \text{ cm}^{-1}$)
30 dominate the total heat transport at low temperatures while contributions of higher-frequency phonons ($> 50 \text{ cm}^{-1}$) does
31 not change significantly with temperature because of its small contribution. In BGSn, however, while a middle-frequency
32 ($50\text{-}100 \text{ cm}^{-1}$) phonons dominate the total heat transport at low temperatures, the contribution of low-frequency phonons
33 ($< 20 \text{ cm}^{-1}$) increases as increasing temperature. For example, the contribution of phonons below 50 cm^{-1} to the total κ_p^{SCP}
34 decreases from 74% at 100 K to 64% at 300 K for BGSi while it increases 15% at 100 K to 53% at 600 K for BGSn.

35 The increase in the contribution of low-frequency phonons with temperature may lead to an intriguing phenomenon.

1 Nanostructuring is a technique to reduce phonon mean-free-path (MFP) and, thus, thermal conductivity for thermoelectric
 2 materials [58–60]. In materials with weak anharmonicity, nanostructuring decreases thermal conductivity more at lower
 3 temperatures because of longer MFPs. Indeed, κ_p^{SCP} of nanostructured BGSi decreases more with decreasing the grain
 4 size at lower temperatures, as shown by solid lines in Fig. 4(a). On the other hand, for BGSn, the reduction of κ_p^{SCP} is
 5 weaker at lower temperatures in most cases because of the large contribution of high-frequency phonons, as shown in Fig.
 6 4(b). This non-trivial trend qualitatively disappears in the total κ being outweighed by contribution from κ_c and κ_{el} when
 7 assuming them to be independent of L_g , however, quantitatively, the deterioration of the nanostructuring effect with
 8 increasing temperature is significantly weakened in BGSn due to the strong anharmonicity.

9 D. Detailed Analysis

10 To gain a deeper insight into the increase in thermal conductivity at low frequency with temperature, phonon properties
 11 were analyzed in more detail. While we call phonons at 0-50 cm^{-1} the low-frequency phonons in the above discussion,
 12 Fig. S2(c) (or Fig. 1(b)) shows that the frequency range of 0-50 cm^{-1} is divided by the flat guest modes around 20 cm^{-1} .
 13 Moreover, Fig. 3(b) shows that modal thermal conductivities increase continuously below 20 cm^{-1} above 100 K while
 14 those at 30-40 cm^{-1} suddenly increases above 300 K. The dip frequency of the spectral $\kappa_p^{\text{SCP}}(T)$ of type-I BGSn around
 15 20 cm^{-1} clearly corresponds to the frequency range of flat guest modes, which is highlighted in Fig. S5. Figures 5(a) and
 16 5(b) show that the flat guest modes, which are explicitly at 6-19 cm^{-1} at 100 K, 12-22 cm^{-1} at 300 K, and 19-27 cm^{-1} at
 17 600 K (see Fig. S5), have small lifetimes and group velocities while phonons with smaller frequencies than those of the
 18 flat guest modes have much larger lifetimes and group velocities. (One can see an aggregations of data shifting to a higher
 19 frequency at the corresponding frequencies with increasing temperature.) Figure 5(a) also shows that phonon lifetimes at
 20 30-40 cm^{-1} increase from 300 to 600 K.

21 To investigate effects of the change in lifetimes and group velocities due to the hardening of guest modes, their
 22 effects were analyzed by calculating a virtual thermal conductivity: $\kappa_{p,q}^{\text{SCP}}(T_c, T_v, T_\tau) = c_q(T_c) \mathbf{v}_q^2(T_v) \tau_q(T_\tau)$. Each property,
 23 namely c_q , \mathbf{v}_q^2 , and τ_q , was calculated with the renormalized phonon dispersion, including the polarization vector and
 24 frequency, by the SCP theory and the Bose-Einstein distribution at a given temperature. The effect of a specific phonon
 25 property can be analyzed by changing the corresponding temperature in $\kappa_{p,q}^{\text{SCP}}(T_c, T_v, T_\tau)$. The corresponding phonon
 26 modes at different temperatures were identified to minimize the sum of inner products of all the corresponding
 27 eigenvectors at each \mathbf{q} -point. Figures 5(c) and 5(d) show changes in the modal thermal conductivity, $\kappa_{p,q}^{\text{SCP}}(T_c, T_v, T_\tau)$, due
 28 to each phonon property at lower temperatures (from 100 to 300 K) and higher temperatures (from 300 to 600 K),
 29 respectively. As shown in Fig. 5(c), the increase in thermal conductivity at 0-10 cm^{-1} at the lower temperature range can
 30 be attributed mainly to increase in lifetime and partially to that in group velocity. From 100 to 300 K, the virtual κ_p^{SCP} at
 31 0-10 cm^{-1} increases by 2.6 times and by 24% because of the increase in lifetime and group velocity, respectively. While
 32 the total κ_p^{SCP} decreases because of the decrease in lifetimes at high frequency ($> 60 \text{ cm}^{-1}$), the increase in group velocities
 33 and lifetimes at low frequencies makes the thermal conductivity decay slower with respect to temperature than the
 34 Klemens model, $\kappa_p(T) \propto T^{-1}$ [61]. At the higher temperatures (from 300 to 600 K), the main factor increasing modal
 35 thermal conductivities whose frequencies are lower than those of guest atoms change from lifetime to group velocity, as

1 shown in Fig. 5(d). κ_p^{SCP} at 10-20 cm^{-1} increases by 44% because of the increase in group velocity while lifetimes do not
 2 change κ_p^{SCP} at the same frequency range. In this temperature range, the increase in lifetimes which appear at 30-40 cm^{-1} ,
 3 which is located between the flat guest modes ($\approx 20 \text{ cm}^{-1}$) and flat modes dominated by framework (40-50 cm^{-1}), may be
 4 more interesting. κ_p^{SCP} at 30-40 cm^{-1} increases by 2.8 times because of the increase in lifetimes. Consequently, in addition
 5 to the increase in thermal conductivity of lower-frequency phonons than the flat guest modes, this abnormal increase in
 6 phonon lifetimes at higher frequencies than that of the guest modes leads to the very slow decay of temperature
 7 dependence of $\kappa(T)$.

8 To gain more insights into the abnormal increase in lifetimes at high temperatures, we focused on a phonon mode
 9 at $> 30 \text{ cm}^{-1}$ whose lifetime increased the most. First, we identified that the lifetime of a phonon mode at $\mathbf{q} = (0.00 \ 0.053,$
 10 $0.37)$ and $\omega = 35 \text{ cm}^{-1}$ at 300 K (see Fig. S5) increased the most from 300 to 600 K (from 1.1 to 7.1 ps). Figures 5(e) and
 11 5(f) show, respectively, the magnitude of the three-phonon coupling matrix element, $|V_3|^2$ term, which is determined by
 12 eigenvectors, frequencies, and atomic masses of the scattered phonons (see Eq. 2) and the $|V_3|^2$ term multiplied by SPS
 13 term at 300 and 600 K. These figures clearly show that the decrease in $|V_3|^2$ leads to the decrease in the scattering rate
 14 and, thus, the increase in the lifetime of the target phonon mode.

15 E. Contribution of Off-diagonal Components

16 Finally, we have analyzed the contribution of coherent thermal transport. Considering this effect, we have reproduced a
 17 slower reduction of thermal conductivity of type-I BGSn above room temperature, as shown in Fig. 2. Figure 6 shows
 18 that flat bands below 60 cm^{-1} mainly contribute to the coherent thermal transport in the overall temperature. Below 60
 19 cm^{-1} , flat modes dominated by the framework (30-60 cm^{-1}) have a larger impact on the coherent component than the flat
 20 guest modes ($\approx 20 \text{ cm}^{-1}$). The figure also shows that coupling between nearly-degenerate states ($\omega_1 \approx \omega_2$) has a large
 21 contribution in the low-frequency range (20-60 cm^{-1}). However, because phonons at this low-frequency range are excited
 22 up to 100 K, $\kappa_c(T)$ below 60 cm^{-1} does not change significantly with increasing temperature above 100 K. Instead of the
 23 low-frequency phonons, the contribution of phonon pairs with different frequencies ($\omega_1 \neq \omega_2$) at higher frequency (> 60
 24 cm^{-1}) increases with temperature. For example, the contribution of phonons above 60 cm^{-1} increases from 31% at 100 K
 25 to 47% at 600 K. In the total lattice thermal conductivity ($\kappa_p^{\text{SCP}} + \kappa_c$), the contribution of the coherent heat transport
 26 increases from 17% at 100 K to 38% at 600 K, which is not negligible.

27 IV. CONCLUSION

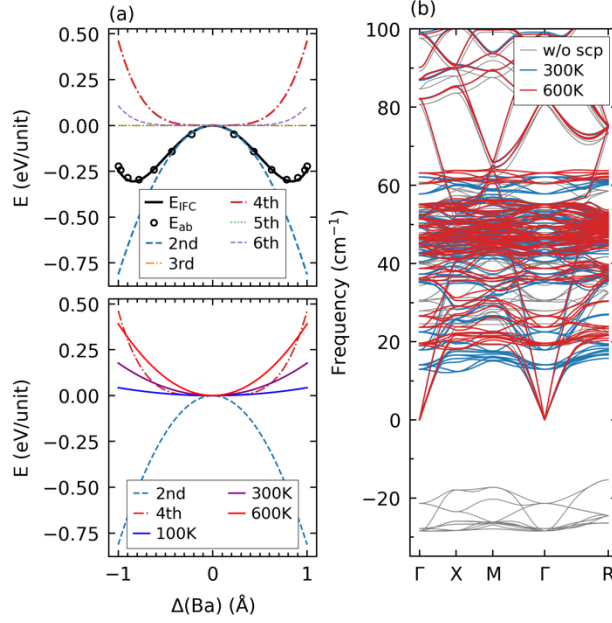
28 In conclusion, we have revealed the complicated effects of strong quartic anharmonicity on phonon properties of a
 29 type-I clathrate with quadruple-well potential. The whole lattice contribution, including interbranch coherent contribution,
 30 was analyzed for lattice contribution by employing first-principles anharmonic lattice dynamics combined with the SCP
 31 theory and the unified theory. The overall trend of the temperature-dependent thermal conductivity, $\kappa(T)$, has been
 32 successfully reproduced by considering electron contribution as well as the lattice contributions. It was confirmed that
 33 the sharp increase in thermal conductivity observed in an experiment can be attributed to electron contribution, bipolar
 34 effect. It was also found that the contribution of the coherent thermal transport is distinct at high temperatures (38% at

1 600 K). More interestingly, we found that lattice thermal conductivity of phonons located at lower frequencies than those
2 of flat bands of the framework ($40\text{-}50\text{ cm}^{-1}$) increases with temperature, and this increase leads to the weak temperature
3 dependence of the total lattice thermal conductivity with increasing temperature.

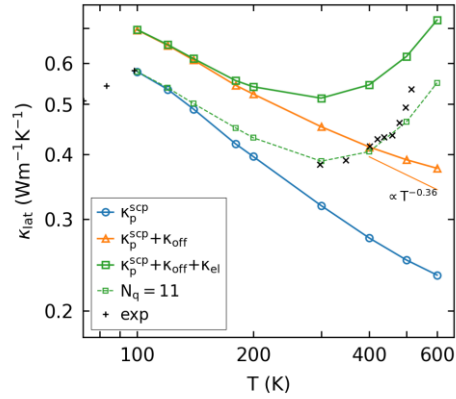
4 Detailed analysis showed that the low-frequency region ($< 40\text{ cm}^{-1}$) can be further divided into two regions by the
5 flat guest modes (T_{2g} and E_g mode around 20 cm^{-1}). The contribution of low-frequency phonons located below the
6 frequency of the guest modes increases with temperature because of the increase in both of group velocities and lifetimes
7 following the hardening of the guest modes. We found that thermal conductivities of phonons with higher frequencies
8 than that of the guest modes start to increase above room temperature (300 K) because of the abnormal increase in their
9 lifetimes. This abnormal increase in the contribution of low-frequency phonons with temperature can be attributed to the
10 decrease in the three-phonon matrix elements, $|V_3|$ terms, with guest modes. These findings indicate that it may be
11 possible to manipulate phonon properties by tuning phonon anharmonicity of materials by using substitutions or
12 vacancies, which can pave a new path of phonon engineering.

13 ACKNOWLEDGEMENTS

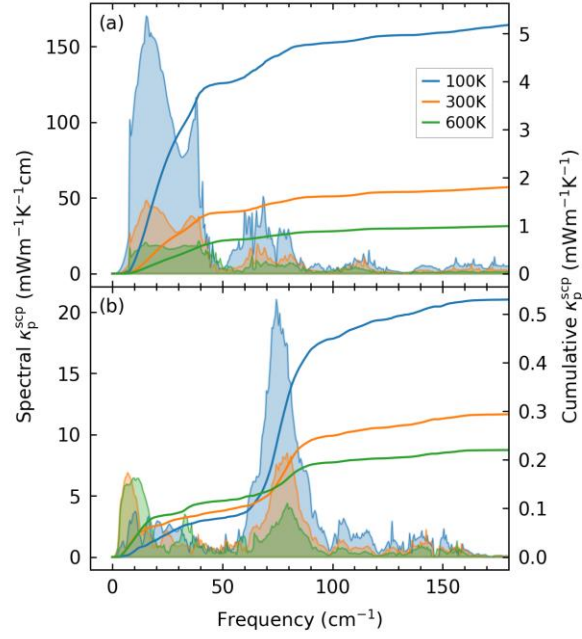
14 The numerical calculations in this work were carried out on the facilities of the Supercomputer Center, Institute for Solid
15 State Physics, the University of Tokyo and MASAMUNE-IMR at Center for Computational Materials Science, Institute
16 for Materials Research, Tohoku University (Project No. 20S0514). This work is partially supported by JSPS KAKENHI
17 Grant No. 19H00744 and No. 20K146761 from Japan Society for the Promotion of Science (JSPS), and CREST Grant
18 No. JPMJCR20Q3 and No. JPMJCR19Q3 from Japan Science and Technology Agency (JST)



1
2 Fig. 1. Temperature-dependent harmonic phonon properties of type-I BGSn. (a) Potential energy surface (PES) of the
3 lowest guest mode at the Γ point (T_{2g} mode). In the top panel, black circles show values obtained directly from first-
4 principles calculations and the black line shows data obtained through the interatomic force constants. Colored lines show
5 PESs decomposed up to sixth-order. In the bottom panel, solid lines show temperature-dependent harmonic potentials.
6 (b) Phonon dispersions obtained without (grey) and with (blue and red) considering the quartic anharmonicity. The latter
7 is shown for 300 and 600 K.



9
10 Fig. 2. Temperature-dependent thermal conductivity of type-I BGSn. Blue, orange, and green lines denote data including
11 the nondiagonal Peierls contribution (κ_p^{SCP}), interbranch coherent contribution (κ_c), and electron contribution (κ_{el}),
12 respectively. Data on the dotted line were obtained with $11 \times 11 \times 11$ q -mesh while other data were with the linear
13 extrapolation with respect to N_q^{-1} . Black markers show experimental data of single crystals obtained from Ref. [31] for
14 temperatures below 100 K and Ref. [40] above 300 K. Note that the experiments were measured by different methods: a
15 steady-state method below 100 K and laser flash above 300 K.

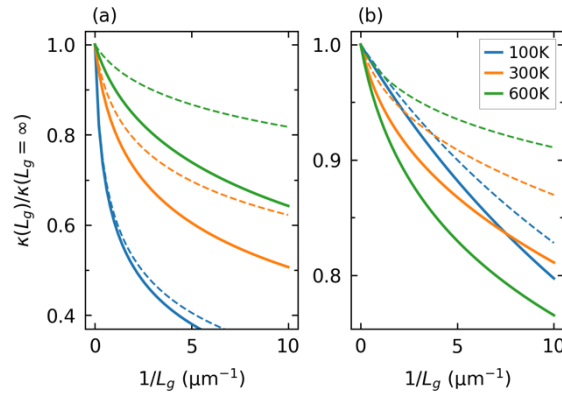


1

2 Fig. 3. Spectral and cumulative lattice thermal conductivities of (a) BGSi and (b) BGSn at different temperatures. The
 3 contribution of interbranch coherent component is not considered.

4

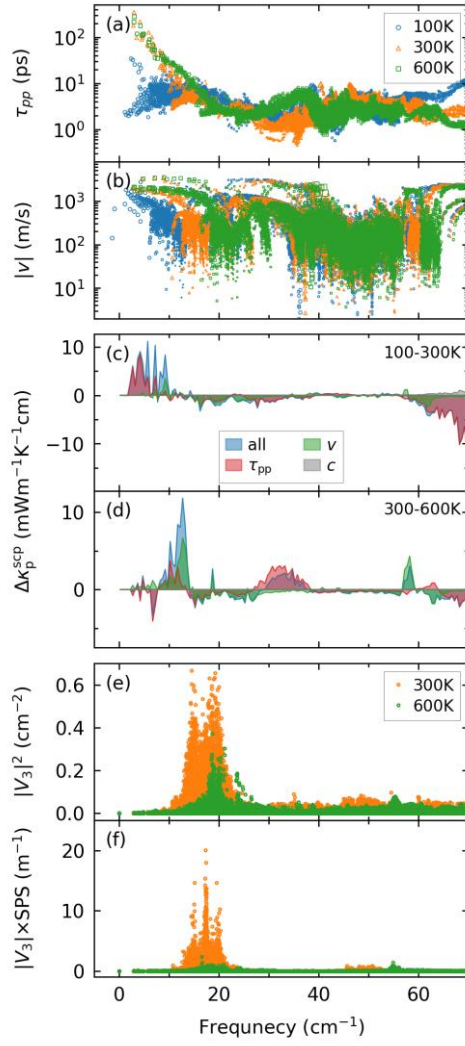
5



6

7 Fig. 4. Decrease in thermal conductivity due to nanostructuring for type-I (a) BGSi and (b) BGSn. Solid and dotted lines
 8 show data for $\kappa = \kappa_p^{SCP}(L_g)$ and $\kappa = \kappa_p^{SCP}(L_g) + \kappa_c + \kappa_{el}$, respectively. It is assumed that κ_c and κ_{el} do not depend on
 9 the grain size, L_g .

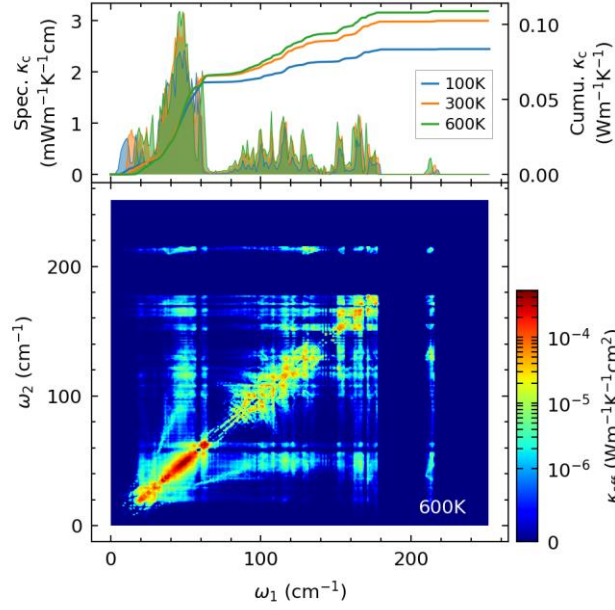
10



1

2 Fig. 5. Effect of hardening of flat guest bands in type-I BGSn. (a) Lifetime due to phonon-phonon scattering and (b) group
 3 velocity at different temperatures. (c), (d) Change in modal thermal conductivities due to different phonon properties
 4 (group velocity, lifetime, and other factors) from (c) 100 to 300 K and (d) 300 to 600 K. Note that phonon frequencies
 5 depend on temperature in the analysis with the SCP theory. In panel (c) and (d), phonon frequencies at 100 and 300 K are
 6 taken, respectively. (e), (f) The magnitude of the three-phonon coupling matrix element, $|V_3|^2$, (e) and $|V_3|^2$ multiplied
 7 by the SPS term (f) of the mode whose lifetime increases the most between 300 and 600 K (from 1.1 to 7.1 ps) that locates
 8 at 35 cm^{-1} and $\mathbf{q} = (0.0, 0.053, 0.37)$ at 300 K (see Fig. S5).

9



1

2 Fig. 6. Contribution of the interbranch coherent component, κ_c , of type-I BGSn. The top panel shows spectral and
 3 cumulative thermal conductivities at different temperatures while the bottom panel shows the two-dimensional modal
 4 thermal conductivity, $\kappa_c(\omega_1, \omega_2)$ (see Eq. (3)). To obtain the spectral and cumulative thermal conductivities (top), the
 5 contribution of a mode q_1 of a coupling between two modes q_1 and q_2 is distributed as $c_{q_1}/(c_{q_1} + c_{q_2})$, where c_q is the
 6 mode specific heat.

7

8

9

10 [1] G. A. Slack, *CRC Handbook of Thermoelectrics* (1995).

11 [2] B. C. Sales, D. Mandrus, B. C. Chakoumakos, V. Keppens, and J. R. Thompson, *Phys. Rev. B* 56, 15081 (1997).

12 [3] T. Tadano and S. Tsuneyuki, *Phys. Rev. B* 92, 054301 (2015).

13 [4] M. A. Haque, S. Kee, D. R. Villalva, W.-L. Ong, and D. Baran, *Adv. Sci.* 7, 1903389 (2020).

14 [5] M. Christensen, A. B. Abrahamsen, N. B. Christensen, F. Juranyi, N. H. Andersen, K. Lefmann, J. Andreasson, C.
 15 R. H. Bahl, and B. B. Iversen, *Nat. Mater.* 7, 811 (2008).

16 [6] T. Takabatake, K. Suekuni, T. Nakayama, and E. Kaneshita, *Rev. Mod. Phys.* 86, 669 (2014).

17 [7] K. Suekuni, M. A. Avila, K. Umeo, and T. Takabatake, *Phys. Rev. B* 75, 195210 (2007).

18 [8] K. Suekuni, M. A. Avila, K. Umeo, H. Fukuoka, S. Yamanaka, T. Nakagawa, and T. Takabatake, *Phys. Rev. B* 77,
 19 235119 (2008).

- 1 [9] M. Christensen, S. Johnsen, and B. B. Iversen, *Dalton Trans.* 39, 978 (2010).
- 2 [10] D. Weaire and R. Fhelan, *Phil Mag Lett* 70, 345 (2006).
- 3 [11] G. S. Nolas, J. L. Cohn, G. A. Slack, and S. B. Schujman, *Appl. Phys. Lett.* 73, 178 (1998).
- 4 [12] J. L. Cohn, G. S. Nolas, V. Fessatidis, T. H. Metcalf, and G. A. Slack, *Phys. Rev. Lett.* 82, 779 (1999).
- 5 [13] B. C. Sales, B. C. Chakoumakos, R. Jin, J. R. Thompson, and D. Mandrus, *Phys. Rev. B* 63, 245113 (2001).
- 6 [14] Y. Takasu, T. Hasegawa, N. Ogita, M. Udagawa, M. A. Avila, K. Suekuni, I. Ishii, T. Suzuki, and T. Takabatake,
7 *Phys. Rev. B* 74, 174303 (2006).
- 8 [15] K. Suekuni, Y. Takasu, T. Hasegawa, N. Ogita, M. Udagawa, M. A. Avila, and T. Takabatake, *Phys. Rev. B* 81,
9 205207 (2010).
- 10 [16] S. Christensen, M. S. Schmøkel, K. A. Borup, G. K. H. Madsen, G. J. McIntyre, S. C. Capelli, M. Christensen, and
11 B. B. Iversen, *J. Appl. Phys.* 119, 185102 (2016).
- 12 [17] C. H. Lee, I. Hase, H. Sugawara, H. Yoshizawa, and H. Sato, *J. Phys. Soc. Jpn.* 75, 123602 (2006).
- 13 [18] W. Li and N. Mingo, *Phys. Rev. B* 89, 184304 (2014).
- 14 [19] T. Tadano, Y. Gohda, and S. Tsuneyuki, *Phys. Rev. Lett.* 114, 095501 (2015).
- 15 [20] T. Tadano and S. Tsuneyuki, *Phys. Rev. Lett.* 120, 105901 (2018).
- 16 [21] X. Zheng, S. Y. Rodriguez, and J. H. Ross, *Phys Rev B* 84, 024303 (2011).
- 17 [22] I. Zerec, V. Keppens, M. A. McGuire, D. Mandrus, B. C. Sales, and P. Thalmeier, *Phys. Rev. Lett.* 92, 185502
18 (2004).
- 19 [23] D. J. Hooton, *Philos Mag* 3, 49 (1958).
- 20 [24] T. Tadano and S. Tsuneyuki, *J. Phys. Soc. Jpn.* 87, 041015 (2018).
- 21 [25] M. Simoncelli, N. Marzari, and F. Mauri, *Nat. Phys.* 395, 1 (2019).
- 22 [26] G. Kresse and J. Furthmüller, *Phys. Rev. B* 54, 11169 (1996).
- 23 [27] J. P. Perdew, K. Burke, and M. Ernzerhof, *Phys. Rev. Lett.* 77, 3865 (1996).

- 1 [28] P. E. Blöchl, Phys. Rev. B 50, 17953 (1994).
- 2 [29] G. Kresse and D. Joubert, Phys. Rev. B 59, 1758 (1999).
- 3 [30] H. Anno, H. Yamada, T. Nakabayashi, M. Hokazono, and R. Shirataki, J. Phys.: Conf. Ser. 379, 012007 (2012).
- 4 [31] M. A. Avila, K. Suekuni, K. Umeo, H. Fukuoka, S. Yamanaka, and T. Takabatake, Appl. Phys. Lett. 92, 041901
5 (2008).
- 6 [32] K. Parlinski, Z. Q. Li, and Y. Kawazoe, Phys. Rev. Lett. 78, 4063 (1997).
- 7 [33] W. G. Hoover, Phys. Rev. A 31, 1695 (1985).
- 8 [34] T. Hastie, R. Tibshirani, and M. Wainwright, *Statistical Learning with Sparsity: The Lasso and Generalizations*
9 (Chapman & Hall/CRC, 2015).
- 10 [35] I. Errea, M. Calandra, and F. Mauri, Phys Rev B 89, 064302 (2014).
- 11 [36] R. J. Hardy, Phys. Rev. 132, 168 (1963).
- 12 [37] S. Tamura, Phys. Rev. B 27, 858 (1983).
- 13 [38] P. E. Blöchl, O. Jepsen, and O. K. Andersen, Phys Rev B 49, 16223 (1994).
- 14 [39] T. Tadano, Y. Gohda, and S. Tsuneyuki, J. Phys.: Condens. Matter 26, 225402 (2014).
- 15 [40] Y. Saiga, K. Suekuni, B. Du, and T. Takabatake, Solid State Commun. 152, 1902 (2012).
- 16 [41] G. K. H. Madsen, J. Carrete, and M. J. Verstraete, Comput. Phys. Commun. 231, 140 (2018).
- 17 [42] See Supplemental Material at [URL].
- 18 [43] F. Oba and Y. Kumagai, Appl. Phys. Express 11, 060101 (2018).
- 19 [44] N. P. Blake, D. Bryan, S. Lattner, L. Møllnitz, G. D. Stucky, and H. Metiu, J. Chem. Phys. 114, 10063 (2001).
- 20 [45] E. N. Nenghabi and C. W. Myles, Phys. Rev. B 77, 205203 (2008).
- 21 [46] M. Ångqvist, D. O. Lindroth, and P. Erhart, Chem. Mater. 28, 6877 (2016).
- 22 [47] M. Ångqvist and P. Erhart, Chem. Mater. 29, 7554 (2017).

- 1 [48] D. O. Lindroth, J. Brorsson, E. Fransson, F. Eriksson, A. Palmqvist, and P. Erhart, Phys. Rev. B 100, 045206
2 (2019).
- 3 [49] T. Mori, K. Iwamoto, S. Kushibiki, H. Honda, H. Matsumoto, N. Toyota, M. A. Avila, K. Suekuni, and T.
4 Takabatake, Phys Rev Lett 106, 015501 (2011).
- 5 [50] J. Shiomi, K. Esfarjani, and G. Chen, Phys. Rev. B 84, 104302 (2011).
- 6 [51] F. Bridges and L. Downward, Phys. Rev. B 70, 140201 (2004).
- 7 [52] L. Xie, J. H. Feng, R. Li, and J. Q. He, Phys Rev Lett 125, 245901 (2020).
- 8 [53] Y. Xia, V. I. Hegde, K. Pal, X. Hua, D. Gaines, S. Patel, J. He, M. Aykol, and C. Wolverton, Phys Rev X 10,
9 041029 (2020).
- 10 [54] M. A. Avila, K. Suekuni, K. Umeo, H. Fukuoka, S. Yamanaka, and T. Takabatake, Phys. Rev. B 74, 125109
11 (2006).
- 12 [55] T. Nakayama and E. Kanashita, Epl-Europhys Lett 84, 66001 (2008).
- 13 [56] D. G. Cahill, S. K. Watson, and R. O. Pohl, Phys. Rev. B 46, 6131 (1992).
- 14 [57] S. Paschen, W. Carrillo-Cabrera, A. Bentien, V. H. Tran, M. Baenitz, Y. Grin, and F. Steglich, Phys. Rev. B 64,
15 214404 (2001).
- 16 [58] B. Poudel, Q. Hao, Y. Ma, Y. Lan, A. Minnich, B. Yu, X. Yan, D. Wang, A. Muto, D. Vashaee, X. Chen, J. Liu,
17 M. S. Dresselhaus, G. Chen, and Z. Ren, Science 320, 634 (2008).
- 18 [59] M. Kashiwagi, Y. Liao, S. Ju, A. Miura, S. Konishi, T. Shiga, T. Kodama, and J. Shiomi, ACS Appl. Energy
19 Mater. 2, 7083 (2019).
- 20 [60] M. Ohnishi and J. Shiomi, APL Mater. 7, 013102 (2019).
- 21 [61] P. G. Klemens, Proc Phys Soc Sect 68, 1113 (1955).
- 22
- 23